

Fast full-body reconstruction for a functional human RPC-PET imaging system using list-mode simulated data and its applicability to radiation oncology and radiology

Paulo Magalhaes Martins^{abc}, Paulo Crespo^{bd}, Miguel Couceiro^{be}, Nuno Chichorro Ferreira^{fg}, Rui Ferreira Marques^{bd}, Joao Seco^{ah} and Paulo Fonte^{be}

^aDepartment of Medical Physics in Radiooncology, German Cancer Research Center - DKFZ, Heidelberg, Germany; ^bLIP - Laboratório de Instrumentação e Física Experimental de Partículas, Physics Department, University of Coimbra, Coimbra, Portugal; ^cInstitute of Biophysics and Biomedical Engineering - IBEB, Faculty of Sciences of the University of Lisbon, Lisbon, Portugal; ^dPhysics Department, University of Coimbra, Coimbra, Portugal; ^ePolytechnic Institute of Coimbra, ISEC, Coimbra, Portugal; ^fIBILI - Institute for Biomedical Imaging and Life Sciences, Faculty of Medicine of the University of Coimbra, Coimbra, Portugal; ^gICNAS - Instituto de Ciências Nucleares Aplicadas à Saúde, University of Coimbra, Coimbra, Portugal; ^hDepartment of Physics and Astronomy, University of Heidelberg, Heidelberg, Germany

ARTICLE HISTORY

Compiled October 22, 2021

ABSTRACT

Background: Single-bed whole-body positron emission tomography based on resistive plate chamber detectors (RPC-PET) has been proposed for human studies, as a complementary resource to scintillator-based PET scanners. The purpose of this work is mainly about providing a reconstruction solution to such whole-body single-bed data collection on an event-by-event basis. We demonstrate a fully three-dimensional time-of-flight (TOF)-based reconstruction algorithm that is capable of processing the highly inclined lines of response acquired from a system with a very large axial field of view, such as those used in RPC-PET. Such algorithm must be sufficiently fast that it will not compromise the clinical workflow of an RPC-PET system.

Material and methods: We present simulation results from a voxelized version of the anthropomorphic NURBS-based cardiac-torso (NCAT) phantom, with oncological lesions introduced into critical regions within the human body. The list-mode data was reconstructed with a TOF-weighted maximum-likelihood expectation maximization (MLEM). To accelerate the reconstruction time of the algorithm, a multi-threaded approach supported by graphical processing units (GPUs) was developed. Additionally, a TOF-assisted data division method is suggested that allows the data from nine body regions to be reconstructed independently and much more rapidly.

Results and Conclusions: The application of a TOF-based scatter rejection method reduces the overall body scatter from 57.1% to 32.9%. The results also show that a 300-ps FWHM RPC-PET scanner allows for the production of a reconstructed image in 3.5 minutes following a 7-minute acquisition upon the injection of 2 mCi of activity (146 M coincidence events). We present for the first time a full realistic reconstruction of a whole body, long axial coverage, RPC-PET scanner. We demonstrate clinically relevant reconstruction times comparable (or lower) to the patient acquisition times on both multi-threaded CPU and GPU.

KEYWORDS

RPC-PET; time-of-flight; parallel computing; lesion detectability

CONTACT Paulo Magalhaes Martins. Email: p.martins@dkfz.de; Address: Department of Medical Physics in Radiooncology, German Cancer Research Center - DKFZ, Heidelberg, Germany; Paulo Crespo. Email: crespo@lip.pt; Address: LIP - Laboratório de Instrumentação e Física Experimental de Partículas, Physics Department, University of Coimbra, Coimbra, Portugal.

1. Background

Single-bed whole-body positron emission tomography based on resistive plate chamber detectors [1] has been proposed for human studies (RPC-PET) [2]. RPC-based detectors offer simple and economical construction, reliability of operation, and extremely good time and intrinsic position resolutions (300 ps full width at half maximum (FWHM) for the coincidence of two 511 keV annihilation photons [2], and 0.4 mm FWHM for a small-animal RPC-PET prototype [3], respectively). The depth-of-interaction (DOI) can also be accurately measured [4], rendering RPC-PET essentially parallax-free. The lack of energy resolution in the RPC-PET detectors is compensated for by their very-high time-of-flight (TOF) resolution and their energy sensitivity [5]. These properties make RPC detectors suitable for large axial field-of-view (AFOV) TOF-PET system.

Fig. 1 illustrates a planned RPC-PET system integrated with a computed tomography (CT) machine. In addition to providing multimodality imaging, the CT will also provide the data necessary to estimate the attenuated and object-scattered events (the latter by simulations [6,7]) and introduce those corrections into the reconstruction.

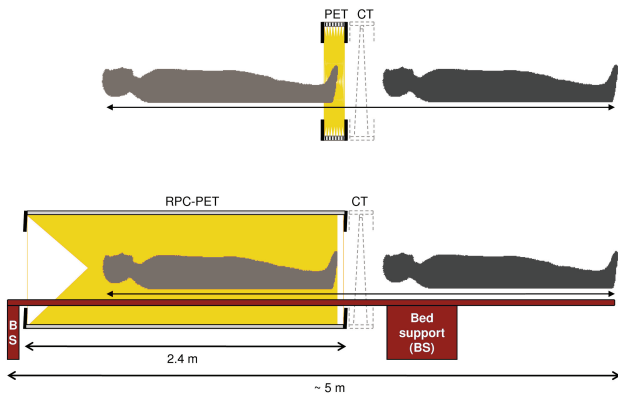


Figure 1. Scheme of the planned RPC-PET system integrated with a CT machine. Detailed transverse and longitudinal views of this RPC-PET system and its detector layout have been presented by Couceiro et al. [8]. The full system length is well within the typical dimensions of current PET-CT rooms utilized for clinical scans. The PET-CT center of the University of Coimbra, for example, has two rooms each with a total length greater than 7 m.

In the last decade, several authors have studied the feasibility of extended-AFOV crystal-based PET scanners [9–12]. However, the high cost of such

systems and the slow performance of reconstruction algorithms remains a major concern.

In this work we address the challenge of providing a reconstruction routine tailored to the potentialities of RPC-PET. Such a routine must process data from the whole AFOV of the system, rather than from one bed at a time as is the case with scintillator-based tomographs with shorter AFOV. In addition, the same routine must be able to incorporate the TOF advantage provided by RPC detectors. At the same time, it must also be fast enough to manage the imaging speed that an RPC-PET system may provide due to its increased sensitivity, which would not only be used to scan faster. It could be used to reduce the injected dose or to have shorter frames in dynamical acquisitions.

The first two aforementioned reconstruction challenges, incoming data from the whole AFOV and capability of TOF processing, were approached by choosing an iterative algorithm capable of processing data in list-mode format: the TOF-weighted maximum-likelihood expectation maximization (MLEM) [13,14]. It was coupled to an attenuation correction procedure developed to accept events from the whole patient body. It is widely accepted today the combination of list-mode acquisition and iterative reconstruction of 3D data, as list-mode storage is more efficient than the binned format for 3D data due to the large number of measured LORs with respect to the number of detected events [15]. List-mode reconstruction methods have greatly improved with the inclusion of both TOF and other physical effects in the system model [16–18]. The highly-computational demands of list-mode reconstruction for shorter AFOV systems has been successfully overcome with fast computers and parallel computing methods demonstrating very impressive reconstruction times [19–22]. With this work we demonstrate a remarkable reconstruction time for large AFOV systems.

2. Materials and Methods

The reconstructed images presented in this article resulted from the application of the RPC-PET reconstruction algorithm to GEANT4 simulated data (versions 9.02 and 9.03). The software-based anthropomorphic NCAT phantom [23] was adapted

to Geant4, including the whole body activity distribution and attenuated photon emissions from the human body, taking into consideration different tissues and densities [24]. This reconstruction was processed with self-designed C, C++ and CUDA routines. The phantom used in the reconstruction was placed on a body-centered parallelepiped volume and final images were reconstructed into a $350 \times 350 \times 1000$ matrix with $2 \text{ mm} \times 2 \text{ mm} \times 2 \text{ mm}$ voxels. The analyzed list-mode outputs were constructed for an RPC-PET system with 120 gaps and a singles detection efficiency to 511 keV perpendicular gamma rays of 19.4% [24]. The output images were analyzed and processed with ROOT (version 5.34.00, CERN, Geneva, Switzerland).

2.1. Simulated activity

2.1.1. Six spheres in a homogeneous background

This study considered six simulated spherical sources placed in a homogeneous background, with a signal-to-background activity ratio of 6:1. The diameter of each sphere was 10 mm with their locations forming a hexagon with 80 mm sides. The phantom was 1.1 m long and had a diameter of 35 cm (volume = 105 L). Assuming fluorodeoxyglucose (^{18}F -FDG) as the decaying solution and a typical body background activity concentration of 2.12 kBq/mL [24], this corresponded to a scan time of 88 s and 20 billion decays. From 142 M detected events, 41 M were true events and the scatter fraction (SF) after the scatter rejection by a 300 ps FWHM TOF resolution was 45.2%, which was explained by the large diameter of the cylinder that in turn corresponded to a patient with a large body mass index (BMI). The axial acceptance angle was restricted to less than 45° , since the gain in sensitivity does not compensate the increase in the SF; this left 36 M true events to be reconstructed.

2.1.2. NCAT anthropomorphic phantom

Typical standard uptake values (SUV) in tissue range between 0.2 and 0.8 g/mL, with this variability being ascribed to variables such as patient weight, blood glucose level, length of uptake period, partial-volume effect, recovery coefficient,

and type of region of interest (ROI) [25]. In this simulation, we assumed a tissue SUV of 0.27 g/mL which, considering a patient weight of 92kg, yielded a tissue activity concentration of 0.21 kBq/mL for an injected activity of 2 mCi. After the typical 1 h waiting time for ^{18}F -FDG uptake, approximately 1 mCi of the administered activity was retained [26]. To study the NCAT anthropomorphic phantom, 1.6×10^{10} decays were considered, which corresponded to an acquisition time of 440 s. The RPC-PET system detected 146 M coincidence events. The axial acceptance angle was restricted to less than 45° and the NCAT phantom was displaced by 256 mm in the direction from head to feet in order to increase the sensitivity in the upper region of the body. After rejecting the scattered events by a 300 ps FWHM TOF resolution, the SF was 32.9% for a total of 49 M true events.

2.1.3. Six lesions in an anthropomorphic phantom

Datasets of lesions with a diameter of 10 mm each were inserted by simulation into the anthropomorphic phantom with a lesion to background activity ratio of 10:1 [27] and placed in the following regions: cervical, sub-clavicular, axillary, inguinal, knee and foot [27]. To determine the events to be simulated in each lesion and

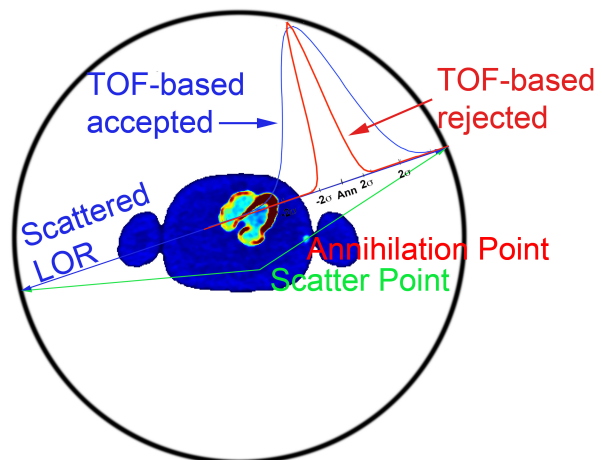


Figure 2. Scheme of the scatter rejection method. The calculated annihilation point located in the scatter LOR has a certain probability of being inside the human body, depending on the TOF resolution. Poorer TOF resolutions (curve in blue) increase the probability of the annihilation point being within the human body, resulting in a TOF-based accepted event. Better TOF resolutions reject a higher fraction of scattered events. The limits of rejection were estimated at the 95% confidence level.

detected by the RPC-PET system, we calculated the time-integrated activity density of the background phantom tissue. This tissue contributed 60% of the total body activity and occupied a volume of 82 L; therefore, it had a time-integrated activity density of 4.4 cts mm⁻³. Consequently, 20.8 k events were simulated for each lesion.

2.2. TOF-based scatter rejection of anthropomorphic events

A method to increase lesion detectability based on the rejection of scattered events by means of their TOF information was investigated.

Fig. 2 illustrates this method by which the annihilation point determined along the scatter line-of-response (LOR) had a certain probability of being inside the human body, according to the TOF resolution. The limits of rejection were estimated at a 95% confidence level. The body outline was determined from knowledge of the NCAT outline and a CT would be used for measured data.

2.3. Multi-threaded GPU-based parallelization reconstruction strategy with a TOF kernel

In this reconstruction, the TOF kernel was modeled as a Gaussian with a kernel of 300 ps FWHM - measured coincidence time resolution, as shown by experimental results with an RPC-PET detector for human PET [2]. This modeling was based on the direct technique for voxel filling [16].

The reconstruction routine consisted of considering a certain number of samples equally spaced inside the 300 ps FWHM TOF Gaussian and giving them the equivalent Gaussian weight, so the sum of the weights equaled one. These samples are centered in the coincidence time difference of the corresponding two annihilation photons detected. Fig. 3 shows the equally spaced samples with their corresponding weights.

The more samples we considered, the lower was their individual weight. For the 16-thread CPU implementation, 15 samples were used while for the GPU implementation, 32 samples were considered without compromising reconstruction speed and image quality. In order to increase the compute-to-memory access ratio, we used the GPU

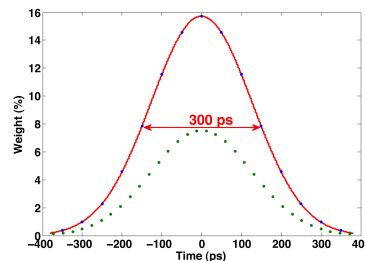


Figure 3. Distribution of the time uncertainty associated with a 300 ps FWHM TOF resolution. The TOF uncertainty along the space variable and its respective weight is distributed along 15 and 32 samples, used for the 16-thread CPU and GPU routine implementations, respectively. These values are accessed through a look-up table (LUT).

constant memory. To overcome the inefficiency of cache entries resulting from having the TOF uncertainties along the space variable and their corresponding weights stored in separate arrays, we arranged the elements of these arrays as a struct, known as an array of structs [28,29].

In a first approach, we gave an equal weight to each sample of the TOF-kernel and this was filled randomly [30], thus consuming undesired computing time capabilities. In the following results, we accessed the 300 ps FWHM Gaussian samples through a look-up table (LUT) containing the TOF uncertainties along the space variable and their respective weights. This approach always generated an identically reconstructed image, in contrast with the random sample generation method. Our studies revealed that the former has increased background noise and the latter serves as a smoothing filter with a small impact on contrast recovery.

The reconstruction routines were both implemented on an NVIDIA Tesla C2075 GPU assisted by a double Intel Xeon E5620 2.4GHz CPU with 16 threads, versus the 16-thread CPUs alone.

2.4. MLEM and OSEM mathematical implementation

The list-mode data were reconstructed by using MLEM that included a TOF probability density function [16]. Attenuation correction was implemented in the forward projection by a weight inversely proportional to the probability of the event being attenuated. The attenuation correction was incorporated neither in the form of the attenuation weighted (AW)-MLEM [31] nor in the

AW-OSEM [32]. It has been shown that implementing the attenuation correction to the LOR is a good approximation for applying a correction in the sensitive matrix [14,33]. The inclusion of a random and TOF-based scatter corrections remained outside the scope of this work.

Sieves [34] (an operation that suppresses high frequency noise) can be applied to the image estimate after each iteration to impose smoothness and reconstruction stability. For this reason, we introduced a median filter between MLEM iterations in our reconstructions routines. In fact, this operation was fundamental for the reconstruction of very low data for such a huge volume. The drawback of this technique is the impact on the reconstruction speed which still remains its bottleneck despite the parallelization of the image regions to be filtered.

2.5. Performance optimization: TOF-assisted data division into different body regions

This method proposed to increase the performance of the reconstruction routine by independently reconstructing nine different regions of the body.

In Fig. 4, we see that for LOR 1 the most probable annihilation location given by a TOF-based calculation ascribed a 40% probability of such an event occurring within image 5, and a 60% probability of such an event having arisen in image region number 6. However, LOR 2 was assigned in its entirety to image region number 7. Even very-inclined LORs (45°) crossing several image spaces, such as LOR 3, always contributed to 1 or 2 image regions provided that the TOF information remained much smaller than the width of each region.

Data incoming from an outer shell of 6 mm in both axial directions to these image regions was added and an overlap between neighbouring regions was performed as is the usual practice in conventional multi-bed systems.

To consider the events laying outside the divided images while iterating on the TOF-kernel, a margin of $\approx 3\sigma$ in the space variable was taken into consideration. In this method, the first image region (feet) is $200 \times 350 \times 350$. The other 8 image regions are $100 \times 350 \times 350$. Image regions 2 to 8 are

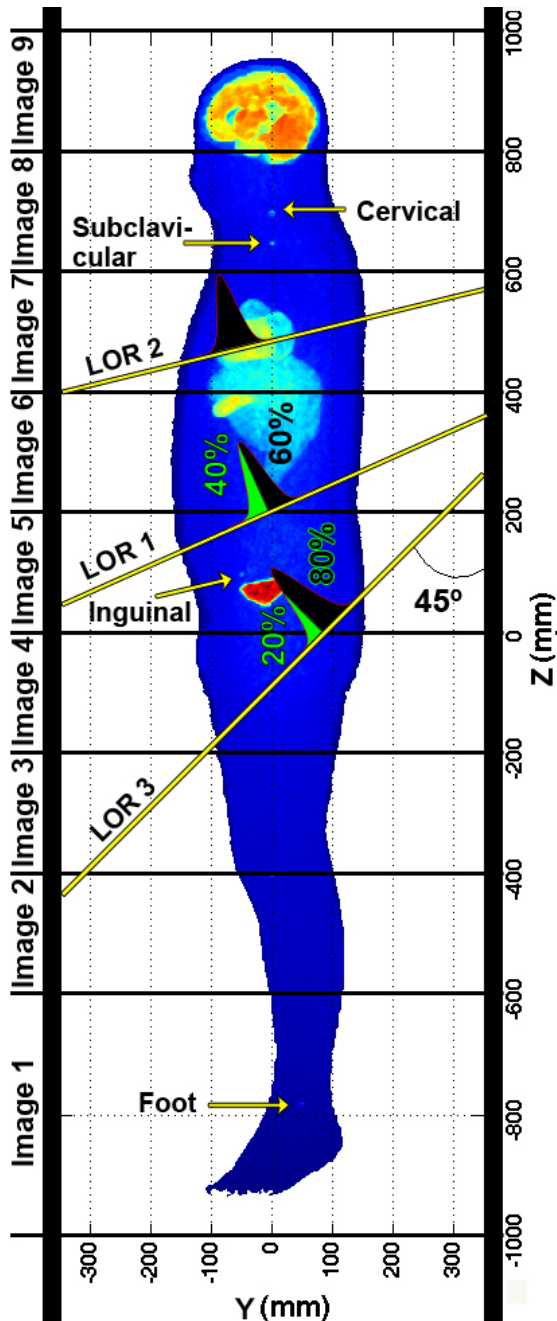


Figure 4. TOF-assisted data division into nine different body regions. This maximum intensity projection (MIP) image clearly shows the inguinal, subclavicular, cervical, and foot lesions. The separation between the inguinal lesion and the bladder is remarkable, as discussed later in the text.

extended to $176 \times 350 \times 350$ ($\sigma = 19.11 \text{ mm} \Rightarrow 76 \text{ mm} = 3.77 \sigma$) to include the tails of the Gaussian TOF kernel filling in both axial directions. Image region number 1 is extended to $240 \times 350 \times 350$ in the upside direction (4.19σ). Image region number 9 is extended to $144 \times 350 \times 350$ in the downside

direction (4.19σ).

The nine different images were then summed, resulting in a single volume similar to the whole-body reconstructed image.

2.6. Contrast recovery coefficient calculation

Following the strategy adopted by [17] to determine the local contrast recovery coefficient (CRC) values, independent reconstructions were performed both on the NCAT simulated data without the inserted lesions assumed as background, and after inserting the lesions by simulation, the latter representing the signal. The Volumes of Interest (VOIs) were drawn for each lesion with the respective diameter on both images and the CRC was calculated as

$$CRC = (H/B - 1)/(a - 1), \quad (1)$$

where H is the average intensity in the lesion VOI, B is the average intensity in the corresponding background VOI, and a is the simulated lesion to background activity ratio of 10:1. The CRC values were calculated for a single realization and their uncertainties were derived from the uncertainties in the region average of the signal and the background [35]. The same procedure was applied to the six spheres in the homogeneous background. In this case, the simulated contrast was 6:1.

3. Results

3.1. Six spheres in homogeneous background

Fig. 5 shows six simulated and reconstructed – after 20 MLEM iterations – spherical sources immersed in a homogeneous background with a signal-to-background activity ratio of 6:1. The reconstruction and simulated phantom show good quantitative agreement between background values despite the lower contrast of the spheres in the reconstructed images and the increased statistical noise and background variability caused by a low statistics dataset.

3.2. Reconstructed images

Fig. 6 shows the results of the RPC-PET reconstruction applied to Geant4 simulated data

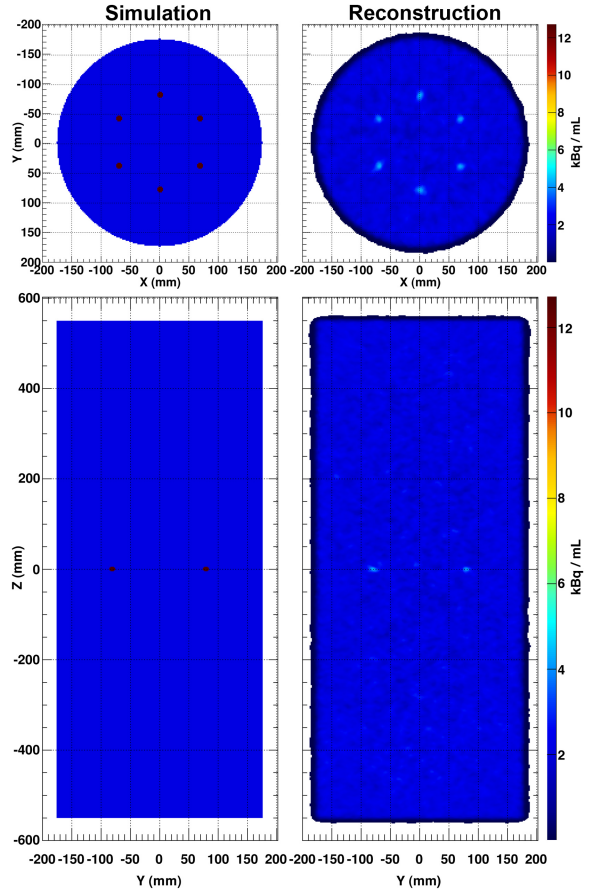


Figure 5. Six simulated and reconstructed spherical sources immersed in a homogeneous activity background. The top images represent the axial view of the cylinder with a 35 cm diameter: simulated emission phantom (left); reconstructed image (right). The bottom row presents the corresponding sagittal views. A cut on the intensity scale was performed on the reconstructed images. The reconstructed image effectively reproduces the simulation phantom, despite the lower visual contrast of the spheres.

based on the NCAT anthropomorphic phantom. The images on the left of Fig. 6 represent the coronal and sagittal views of the NCAT simulation phantom. The images on the right of the same figure show the reconstruction images of 49 M true events after 20 MLEM iterations. A lower cut on the intensity scale and on the following reconstructed images was performed in order to remove the very-low intensity from voxels filled with the tails of the Gaussian TOF kernel.

Axial, coronal and sagittal views of the brain are also included in Figs. 7 and 8 demonstrating the capabilities of RPC-PET to reveal the detailed structures of the brain.

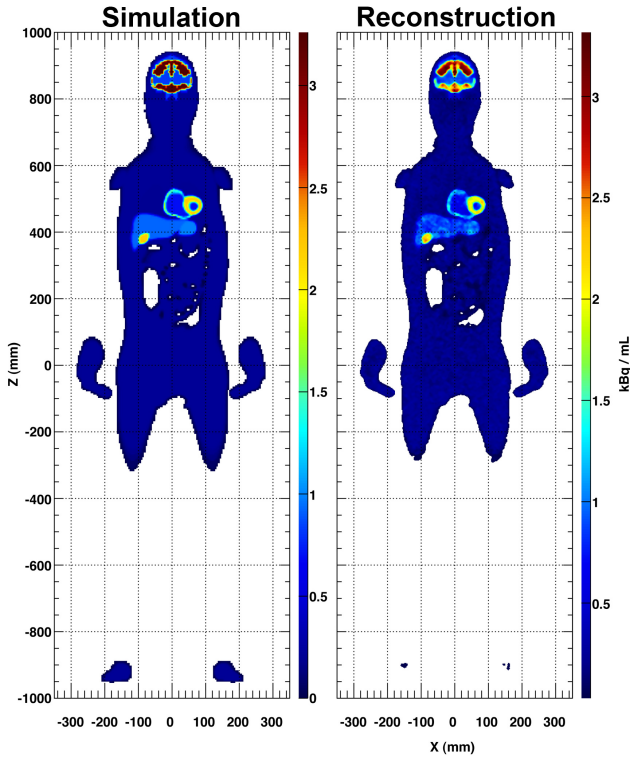


Figure 6. Results of the RPC-PET reconstruction applied to Geant4 simulated data based on the NCAT anthropomorphic phantom (left column). The right column shows reconstructed results after 20 MLEM iterations. The two views represent 2 mm thick slices across the heart region. The sagittal view shows the left ventricle, stomach, spleen and kidney, while the coronal view shows both ventricles of the heart well separated from the liver and stomach. Gallbladder and intensity depressions on the intestine region are also visible.

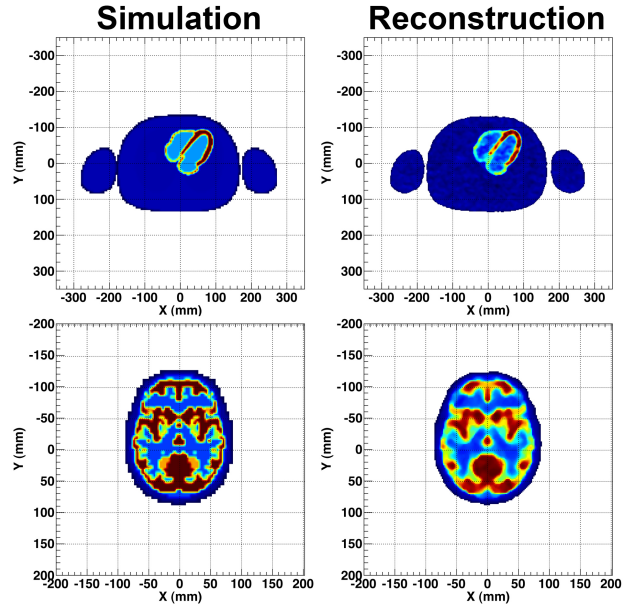


Figure 7. Two-millimeter-thick axial slices of the brain and the heart. This reconstruction offers very high resolution images of the heart walls and the brain regions simultaneously.

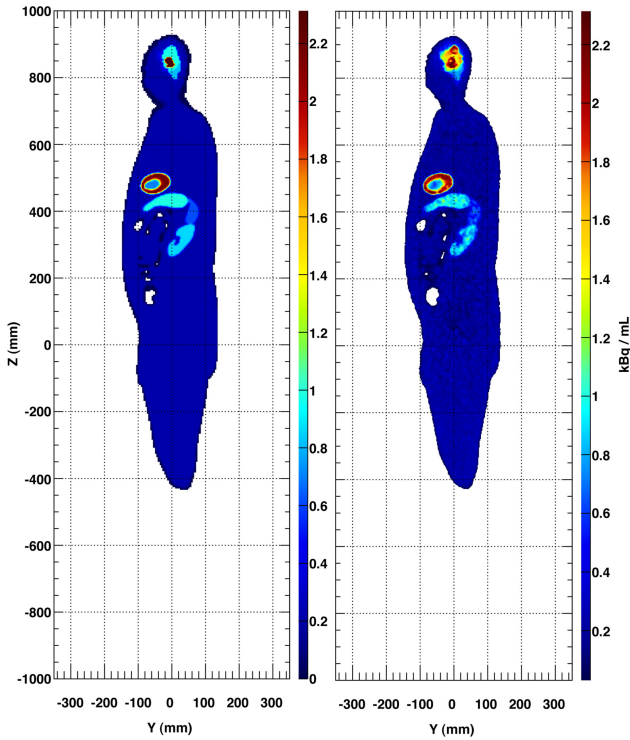


Figure 8. Coronal and axial views of the brain. A very good agreement between the cerebellum and other activated regions of the brain is observed, revealing detailed structural information of the brain.

3.3. Scatter Rejection Fraction

Fig. 9 shows that the lack of energy resolution in the RPC-PET detectors is compensated for by their very-high TOF resolution. Indeed, by applying the scatter rejection method described in section 2.2 (Fig. 2), one sees in Fig. 9 a SF of 32.9% for 300 ps FWHM, which compares with a SF of 57.1% if no scatter rejection by TOF was applied. The scatter rejection fraction (SRF), i.e., the ratio between the number of scattered events rejected with TOF and the total of scattered events detected, was 63% for a 300 ps FWHM TOF resolution. More than half of the scattered LORs did not cross the NCAT

phantom and were therefore also rejected by this method, even for a 4 ns TOF resolution.

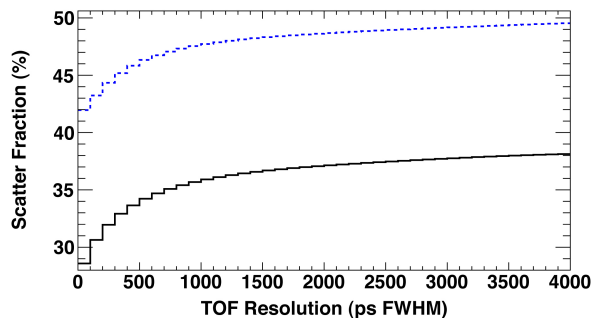


Figure 9. Curve of the body scatter fraction (SF) for a decreasing TOF resolution, calculated for the homogeneous cylindrical phantom (dashed blue) and for the NCAT phantom (solid black). For a 300 ps FWHM TOF resolution, the SF is 32.9% and 45.2% for the homogeneous cylindrical phantom and the NCAT phantom, respectively. For a 600 ps FWHM TOF resolution, these values increase to 34.7% and 46.7%, respectively.

In the case of the spheres immersed in a water phantom, the SF decreased from 67.2% (no TOF) to 45.2% with a 300 ps FWHM TOF-based scatter rejection.

3.4. Six lesions in an anthropomorphic phantom: towards lesion detectability

Fig. 10 shows two sets of 2-mm-thick slice images, each with five simulated lesions. All figures hereinafter presented containing the three views of the five lesions were normalized to 80% of the maximum intensity in the brain. In Fig. 10, we included the true and body-scattered events detected by an RPC-PET system with 120 gaps after passing by an energy selection curve [24]. We then compared the 300 ps and 600 ps FWHM TOF kernels after performing the TOF-based scatter rejection (see Fig. 2). The comparison with the 600 ps FWHM TOF case was in line with the state-of-the-art commercial PET scanners.

Compared to the reconstructed images after performing the rejection cuts with a 600 ps FWHM TOF kernel (Fig. 10, bottom), all the lesions observed in the 300 ps FWHM images (Fig. 10, top) had improved visual contrast, primarily the inguinal lesion, which was almost indistinguishable using the 600 ps FWHM TOF kernel. The contribution of the scatters in the abdomen region was highly suppressed. Therefore, the combination of an RPC-PET detector with a higher TOF resolution

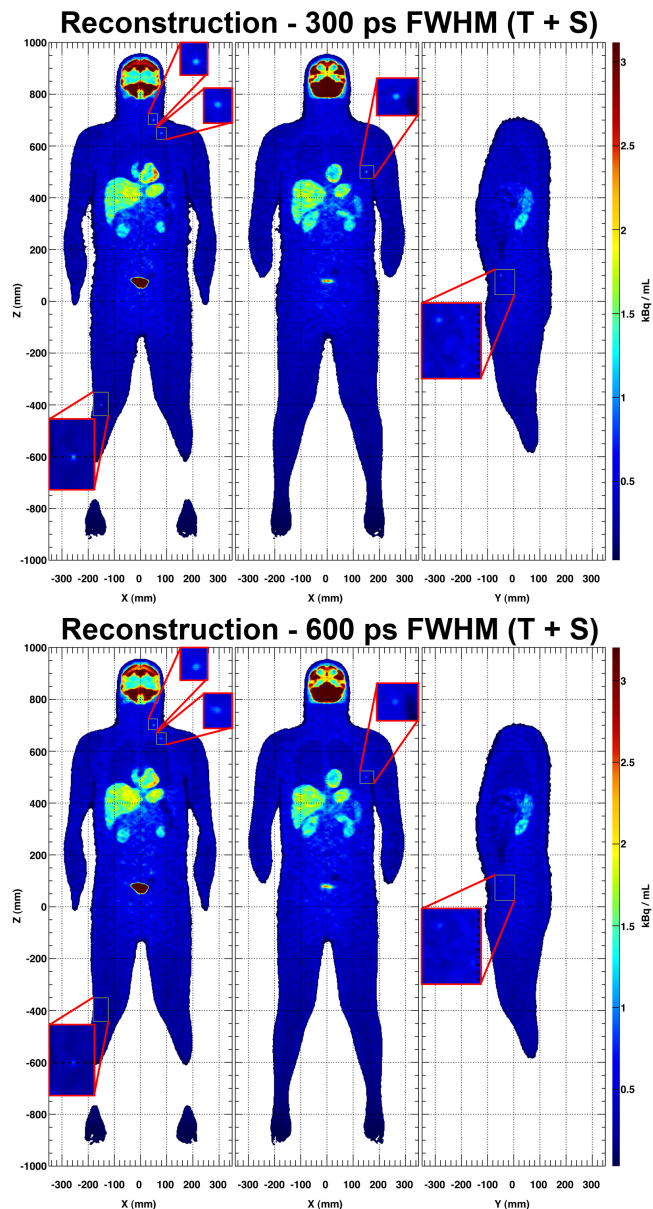


Figure 10. Whole-body 2-mm-thick slice images showing five lesions: cervical, sub-clavicular, knee, axillary, and inguinal. The reconstructed results were obtained from the data (trues and scatters) detected by an RPC-PET system for a 300 ps (top) and a 600 ps (bottom) FWHM TOF kernel. It is a well-known fact that the abdominal region is more contaminated by scatters; however, this region becomes cleaner due to the scatter rejection properties of RPC-PET. The organs are still well separated: the heart from the stomach and the right kidney from the liver. The spleen is still visible. The visual contrast improves in all lesions for a 300 ps FWHM TOF resolution (top), primarily the inguinal one, which is almost indistinguishable with a 600 ps FWHM TOF resolution (bottom). Images were obtained after 20 MLEM iterations. A windowing on the intensity scale was performed to distinguish the lesions.

increases visual detectability, mainly in regions more sensitive to the contribution of scattered events, such as those closer to the abdomen. A more

comprehensive study of the contrast recovery for each lesion will be partly presented in the following sections.

To better distinguish each of the six lesions we show the corresponding axial slices crossing the maximum intensity voxel of each lesion in Fig. 11. The line profiles across the lesion are presented in Fig. 11 (bottom). They discriminate the presence of a lesion in all six cases, including the inguinal one, whose visual detection was not fully evident in the coronal and sagittal views in Fig. 10. This is due to its location in the outer region of the abdomen, where contaminating background is less prominent than in the center.

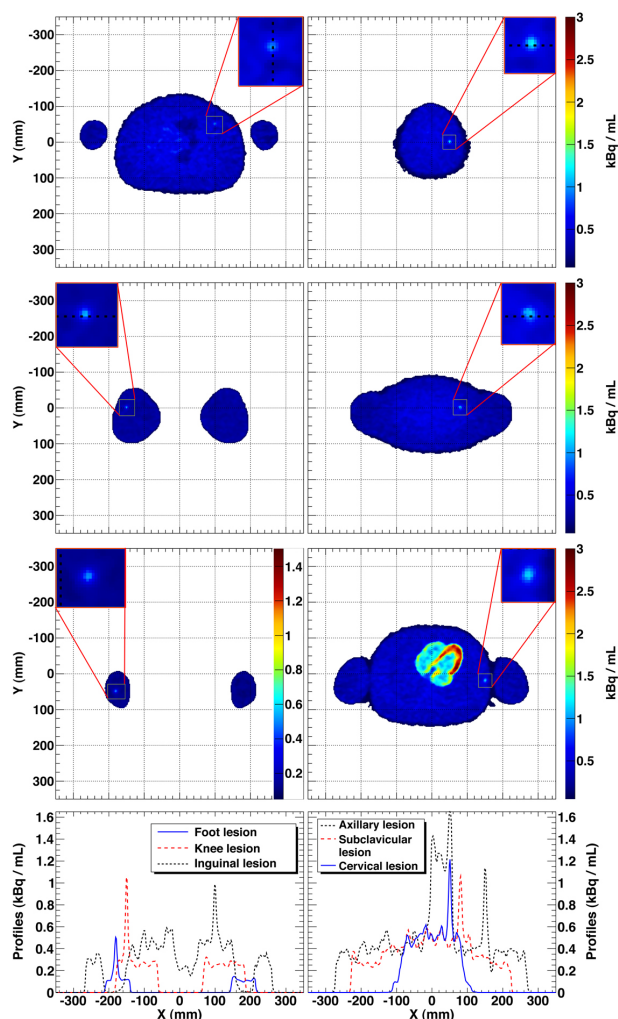


Figure 11. Axial views corresponding to 2 mm thick slices crossing the six lesions. In the left column are shown the foot (bottom); knee (middle); and inguinal (top) lesions. In the right column are shown the axillary (bottom); subclavicular (middle); and cervical (top) lesions. The profile across the inguinal lesion (dashed black curve) clearly indicates the presence of a lesion.

The knee lesion had the best visual contrast, while the axillary lesion appeared with good visual contrast despite the nearby heart within the image. All images, except the one containing the foot lesion, were normalized to the maximum activity in the heart. The foot lesion lost activity due to its presence in the extremity of the RPC detection system (not covered by the whole solid angle acceptance) and was then normalized to half of the maximum intensity in the heart walls.

3.5. Performance

3.5.1. RMSE Evolution

Fig. 12 presents the RMSE evolution for the MLEM reconstruction along 200 iterations for the NCAT (top), and along 80 iterations for the spheres in a homogenous background (bottom).

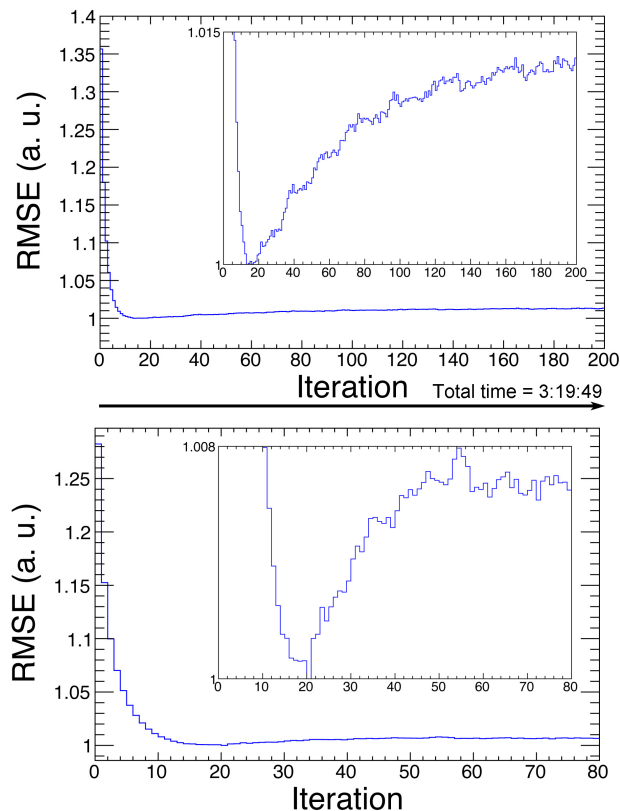


Figure 12. Graph of the evolution of the RMSE along 200 iterations calculated between the NCAT simulated image and the reconstructed true events image (top) and along 80 iterations calculated between the mathematical image of the spheres in a homogeneous background and the reconstructed true events image (bottom). In both, the minimum is reached after 20 iterations.

The RMSE was calculated between the simulated (NCAT) or mathematical image (water cylinder) and the reconstructed true events image. Reconstruction with scattered events was not considered, due to a consequent bias, since scatter correction was not performed. The RMSE reached a minimum after 20 iterations, a fact that led us to the decision of stopping the reconstruction at iteration 20 (in this study).

3.5.2. Image Division

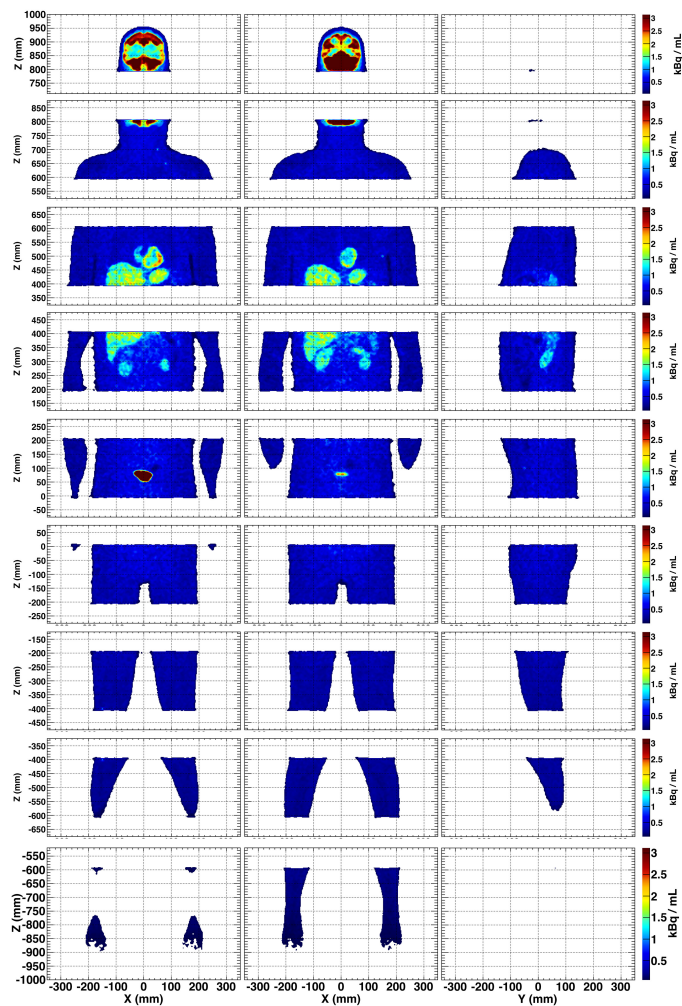


Figure 13. Reconstruction method based on the division of the data through nine different regions of the body. This image represents the nine independent reconstructions, obtained after 20 MLEM iterations. This strategy allows for the full whole-body reconstruction to be performed in only 3.5 minutes, which compares with 21 minutes if the whole body is considered.

As an alternative approach to a whole-body reconstruction, we divided the reconstructed image

based on the data arising from nine different regions of the body. Fig. 13 presents the results of the nine independent reconstructions after 20 MLEM iterations, whose resulting images were then summed and are shown in Fig. 14. This method improved the reconstruction speed as presented later in table 2. A margin of 3σ (as explained in section 2.5) had to be given in order to consider the events laying outside the image while iterating on the TOF-kernel.

A median filter tends to reduce the intensity in a voxel if several surrounding voxels are null, which occurs in the borders of those divided images. Therefore, an outer shell of 6 mm (3 voxels in both Z-directions) was added and an overlap between neighbouring images was performed.

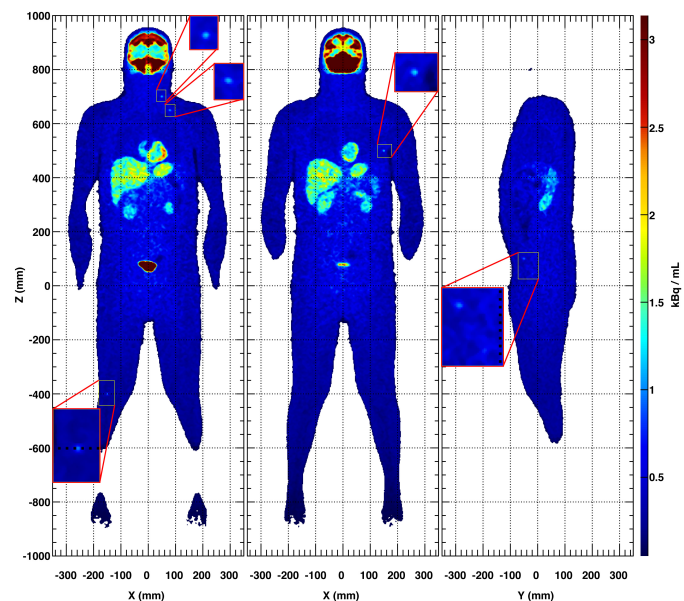


Figure 14. Reconstructed image resulting from the sum of the nine independent reconstructions depicted in Fig. 13. There is no difference to the whole-body reconstruction shown in Fig. 10 (top).

As depicted in Fig 15 (left), the knee lesion positioned in the divided image borders is not affected by this method and its profile (bottom left) compares well with the one in Fig. 11.

This image division method also allowed a quick detection of unexpected lesions, like the one in the foot presented in Fig. 15 (right). Even for this region, in which the RPC-PET detector was less sensitive, the lesion was clearly visible, mainly due to the absence of other surrounding organs with higher uptake values.

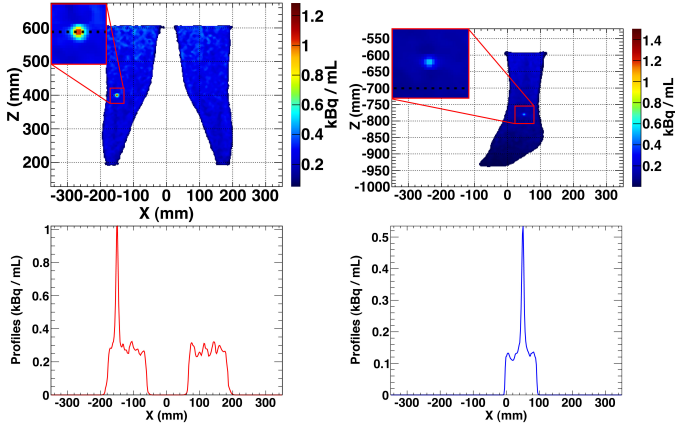


Figure 15. Reconstructed images of the legs (left) and the right foot (right). The activity in the inner part of the leg where the two images sum is not affected and the lesion is well visible. Performing an analysis of each of the nine independent reconstructions, it is possible to detect a lesion in the foot that could go undetected in a whole-body reconstruction due to the lack of intensity in this region with respect to the rest of the body, the latter being fully covered by the solid angle of the RPC-PET system.

3.5.3. Contrast recovery coefficients

The CRC values for the six spheres in the homogeneous phantom obtained from the reconstruction of the true events, with a TOF resolution of 300 ps FWHM, and at iteration 20 (MLEM) are presented in table 1.

Table 1. CRC values for six spheres in homogeneous phantom (%)

Spheres	Trues (300 ps)					
	1	2	3	4	5	6
Iter. 20	18.1 ± 2.0	19.4 ± 2.1	24.3 ± 3.6	17.7 ± 2.0	22.0 ± 2.4	16.0 ± 1.4

We verified that the CRC values for the lesions in the NCAT phantom obtained with the GPU and the 16-thread CPU implementations of the reconstruction routines were quite similar (not shown).

As seen in Fig. 16, there was a large gain between iterations 1 and 20 and a stabilization with an increasing number of iterations.

We present the CRC in the foot, knee and inguinal lesions (top). The CRC took into account the region average for each lesion. The CRC values in other lesions evolved similarly, i.e., they stabilized after iteration 20 (not shown). The advantage of a TOF resolution of 300 ps FWHM is clear for the axillary lesion (bottom).

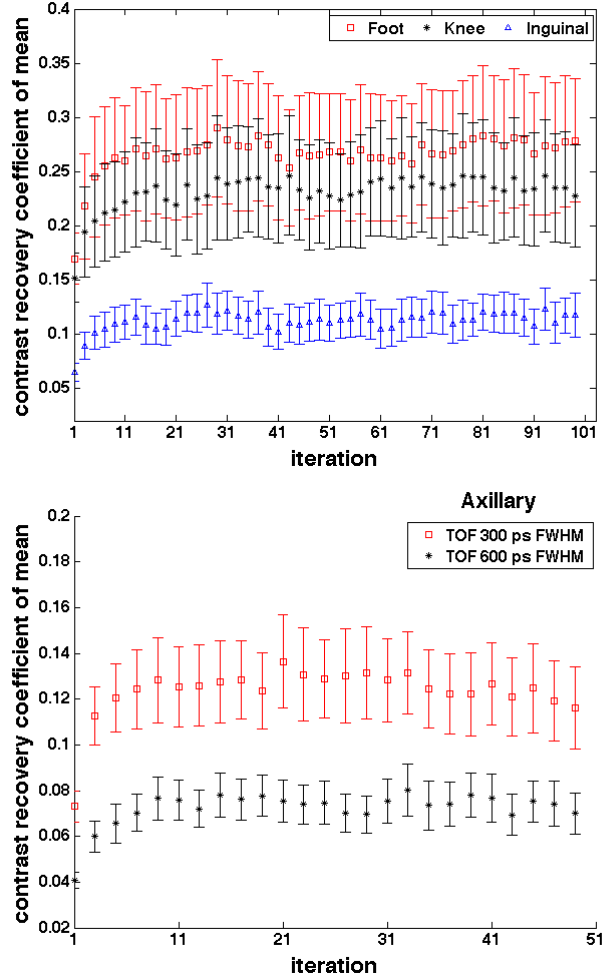


Figure 16. Contrast recovery coefficient evolution with iterations for the images reconstructed with true and scatter events (MLEM, SRF (300 ps FWHM)). Top: CRC in foot, knee and inguinal lesions. Bottom: comparison between a TOF resolution of 300 and 600 ps FWHM for the axillary lesion.

3.5.4. Speed

For the pre-processing and the starting backprojection that feeds the reconstruction routines, we selected 16-thread CPUs alone because the time gain for the GPU implementation of those routines was not remarkable.

The reconstruction times presented in table 2 already took into account the contribution of the pre-processing and backprojection times. Both reconstruction routines ran faster with the GPU plus 16-thread CPU implementation than with the 16-thread CPUs alone.

Table 2 also presents the reconstruction time for the presented images, taking into account the two

different approaches: the whole-body and division methods. For the whole-body, GPU took 21:11 to perform the reconstruction of the data for the SRF (300 ps FWHM).

Considering the image division approach, a performance time below 4 minutes (3:33, 20 iterations) for the superior torso region was accomplished – the worst case in terms of computational burden. This time included the total image reconstruction process.

4. Discussion

The large AFOV and the 300 ps FWHM TOF resolution were combined in the RPC-PET to make this detector relevant for low injection doses and short scan periods. We expect to obtain the images presented in this work with a 7 minute scan and an injected activity of 2 mCi, a value well below the activities currently administered to patients (10 to 20 mCi).

A reconstruction routine capable of providing images for RPC-PET technology was created. A direct TOF implementation of the MLEM algorithms allows for all events to be directly processed and inserted inside the object image by means of a TOF kernel, while handling list-mode data iteratively. A proper attenuation correction was successfully implemented.

A method of rejection of the scattered events was presented, leading to a reduction of the body scatter fraction from 57.1% to 32.9% for a 300 ps FWHM TOF whole-body RPC-PET system.

To study the potential of TOF resolution on lesion detectability, we evaluated its impact on the detection of six simulated lesions spread over critical regions within the anthropomorphic phantom. Lesions close to the abdomen, such as the inguinal lesion, are harder to detect. In comparison with a 600 ps FWHM TOF detector (current commercial crystal-based PET scanners), the 300 ps FWHM whole-body RPC-PET may be a more sensitive detector, representing a potential increase in detectability.

As an alternative approach to whole-body reconstruction, a method based on the division of the data through nine different regions was proposed, resulting in an enhancement in the reconstruction performance. The proposed method provided a reconstruction that was six times faster.

Table 2. Reconstruction time (minutes) for the presented images. Timing in bold indicates largest computing time.

		SRF (300 ps) - Body divided into nine regions			
Body Region		Head Superior	Head Inferior	Torso Superior	Torso Inferior
Pre-process.	Scatter Rejection	0:06	0:02	0:05	0:04
	Attenuation correction	0:06	0:03	0:05	0:04
	Total	0:12	0:05	0:10	0:08
Backprojection		0:14	0:11	0:13	0:13
MLEM 20 it.	16-thread CPUs	4:13	3:38	4:44	4:28
	GPU (Tesla C2075)	3:30	2:48	3:33	3:14

		SRF (300 ps) - Body divided into nine regions				
Body Region		Abdominal Superior	Abdominal Inferior	Legs Superior	Legs Inferior	Feet
Pre-process.	Scatter Rejection	0:03	0:03	0:03	0:02	0:02
	Attenuation correction	0:04	0:03	0:03	0:02	0:01
	Total	0:07	0:06	0:06	0:04	0:03
Backprojection		0:13	0:11	0:10	0:10	0:12
MLEM 20 it.	16-thread CPUs	4:20	4:06	3:51	3:32	3:51
	GPU (Tesla C2075)	3:04	2:51	2:36	2:22	2:40

		Whole Body			
		SRF (300 ps)	SRF (600ps)	Trues (300 ps)	Trues (600 ps)
Pre-process.	Scatter Rejection	0:27	0:44	-	-
	Attenuation correction	0:41	0:52	0:25	0:25
	Total	1:08	1:36	0:25	0:25
Backprojection		1:40	2:16	1:20	1:53
MLEM 20 it.	16-thread CPUs	33:52	-	27:00	-
	GPU (Tesla C2075)	21:11	-	17:03	-

Making use of GPUs assisted by 16-thread CPUs, we expect to reach a reconstructed image from a 300 ps FWHM RPC-PET scanner in 3.5 minutes after the end of data acquisition. Compared to our first attempts to reconstruct whole-body data in a single CPU, which took approximately 90 hours, this represents a significant progress.

A CRC analysis corroborates the conclusions we have drawn thus far: the CRC stabilizes at iteration 20; the inner lesions in the body have a higher loss of contrast due to the contribution of the scattered events in those regions; the TOF resolution dictates the largest contribution to contrast gain.

5. Conclusion

A reconstruction routine capable of providing images for single-bed whole-body RPC-PET technology was demonstrated. An enhancement of reconstruction speed was provided, as well as a method for body-scatter rejection. Future work includes appropriate random and scatter corrections and experimental phantom studies.

Acknowledgments

The authors greatly acknowledge support from the High Performance Computing Center of the University of Coimbra, Portugal, from Dr. Miguel Oliveira former LIP member, from the LIP helpdesk, Gonçalo Borges and João Martins, and from João Silva (LIP). The authors also thank Prof. Dr. Paul Segars, from Johns Hopkins University, for providing the software-based anthropomorphic phantom. This work was supported by the EU, FEDER, POCI, QREN, COMPETE, POFC, PORC, MaisCentro and by the Portuguese Government through Foundation for Science and Technology (FCT) and Comissão de Coordenação e Desenvolvimento Regional do Centro (CCDRC), under the contracts CERN/FP/123605/2011, PTDC/SAU-BEB/104630/2008 and CENTRO-07-ST24-FEDER-002007 (project Rad4Life), co-funded by the European Social Fund and by POPH - Programa Operacional Potencial Humano. P. Crespo, M. Couceiro, and P. Martins acknowledge FCT grants numbers SFRH/BPD/39223/2007, SFRH/BD/42217/2007, and SFRH/BPD/103655/2014, respectively.

Disclosure statement

The authors report no conflicts of interest. The authors alone are responsible for the content and writing of this article.

References

- [1] Fonte P, Smirnitsky A, Williams MCS. A new high-resolution TOF technology. *Nucl Instrum Meth A*. 2000;443(1):201–204.
- [2] Blanco A, Chepel V, Ferreira Marques R, et al. Perspectives for positron emission tomography with RPCs. *Nucl Instrum Meth A*. 2003;508:88–92.
- [3] Martins P, Blanco A, Crespo P, et al. Towards very high resolution rpc-pet for small animals. *Journal of Instrumentation*. 2014;9(10):C10012.
- [4] Blanco A, Carolino N, Correia CMBA, et al. RPC-PET: A new very high resolution PET technology. *IEEE Trans Nucl Sci*. 2006;53(5):2489–2494.
- [5] Blanco A, Couceiro M, Crespo P, et al. Efficiency of RPC detectors for whole-body human TOF-PET. *Nucl Instrum Meth A*. 2009;602(3):780–783.
- [6] Werner ME, Surti S, Karp JS. Implementation and evaluation of a 3D PET single scatter simulation with TOF modeling. In: *Conf. Record of the 2006 IEEE Nucl. Sci. Symp. & Med. Imag. Conf. (NSS/MIC)*; Vol. 3; Oct; San Diego, CA, USA; 2006. p. 1768–1773.
- [7] Watson CC. Extension of single scatter simulation to scatter correction of time-of-flight PET. *IEEE Trans Nucl Sci*. 2007 Oct;54(5):1679–1686.
- [8] Couceiro M, Crespo P, Mendes L, et al. Spatial resolution of human RPC-PET system. *Nucl Instrum Meth A*. 2012;661, Supplement 1(0):S156 – S158.
- [9] Crosetto DB. The 3D complete body screening (3D-CBS) features and implementation. In: *Conf. Record of the 2003 IEEE Nucl. Sci. Symp. & Med. Imag. Conf. (NSS/MIC)*; Vol. 4; Oct; Portland, OR, USA; 2003. p. 2415–2419.
- [10] Eriksson L, Townsend DW, Conti M, et al. Potentials for large axial field of view positron camera systems. In: *Conf. Records 2008 IEEE Nucl. Sci. Symp. & Med. Imag. Conf. (NSS/MIC)*; Oct. 19–25; Dresden, Germany; 2008. p. 1632–1636.
- [11] Borasi G, Fioroni F, Del Guerra A, et al. PET systems: the value of added length. *Eur J Nucl Med Mol Imaging*. 2010;37(9):1629–1632.
- [12] Poon JK, Dahlbom ML, Moses WW, et al. Optimal whole-body PET scanner configurations for different volumes of LSO scintillator: a simulation study. *Phys Med Biol*. 2012;57(13):4077.
- [13] Shepp L, Vardi Y. Maximum likelihood reconstruction for emission tomography. *IEEE Trans Med Imaging*. 1982 Oct;1(2):113–122.
- [14] Groiselle CJ, Glick SJ. 3D PET list-mode iterative reconstruction using time-of-flight information. In: *Conf. Record of the 2004 IEEE Nucl. Sci. Symp. & Med. Imag. Conf. (NSS/MIC)*; Vol. 4; Oct; Rome, Italy; 2004. p. 2633–2638.
- [15] Karp JS, Surti S, Daube-Witherspoon ME, et al. Benefit of time-of-flight in PET: experimental and clinical results. *J Nucl Med*. 2008;49:462–470.
- [16] Crespo P, Shakirin G, Fiedler F, et al. Direct time-of-flight for quantitative, real-time in-beam PET: a concept and feasibility study. *Phys Med Biol*. 2007; 52:6795–6811.
- [17] Daube-Witherspoon ME, Matej S, Werner ME, et al. Comparison of list-mode and DIRECT approaches for

- time-of-flight PET reconstruction. *IEEE Trans Med Imag.* 2012 July;31(7):1461–1471.
- [18] Conti M, Eriksson L, Westerwoudt V. Estimating image quality for future generations of TOF PET scanners. *IEEE Trans Nucl Sci.* 2013 Feb;60(1):87–94.
- [19] Pratz G, Chinn G, Olcott PD, et al. Fast, accurate and shift-varying line projections for iterative reconstruction using the GPU. *IEEE Trans Med Imaging.* 2009 March;28(3):435–445.
- [20] Pratz G, Surti S, Levin CS. Fast list-mode reconstruction for time-of-flight PET using graphics hardware. *IEEE Trans Nucl Sci.* 2011 Feb;58(1):105–109.
- [21] Cui J, Pratz G, Prevrhal S, et al. Fully 3D list-mode time-of-flight PET image reconstruction on GPUs using CUDA. *Medical Physics.* 2011;38(12):6775–6786.
- [22] Sportelli G, Ortuño JE, Vaquero JJ, et al. Massively parallelizable list-mode reconstruction using a Monte Carlo-based elliptical Gaussian model. *Medical Physics.* 2013;40(1):012504.
- [23] Segars WP. Development of a new dynamic NURBS-based cardiac-torso (NCAT) phantom [dissertation]. The University of North Carolina, USA; 2001.
- [24] Crespo P, Reis J, Couceiro M, et al. Whole-body single-bed time-of-flight RPC–PET: simulation of axial and planar sensitivities with NEMA and anthropomorphic phantoms. *IEEE Trans Nucl Sci.* 2012;59(3):520–529.
- [25] Paquet N, Albert A, Foidart J, et al. Within-patient variability of 18F-FDG: standardized uptake values in normal tissues. *Journal of Nuclear Medicine.* 2004; 45(5):784–788.
- [26] Swanson DP, Chilton HM, Thrall JH. *Pharmaceuticals in medical imaging.* New York: Macmillan Publishing Company; 1990.
- [27] Zhang J, Olcott PD, Chinn G, et al. Study of the performance of a novel 1 mm resolution dual-panel PET camera design dedicated to breast cancer imaging using Monte Carlo simulation. *Medical Physics.* 2007;34(2):689–702.
- [28] Kirk DB, Hwu WW. *Programming massively parallel processors.* Massachusetts: Morgan Kaufmann; 2010.
- [29] Sanders J, Kandrot E. *Cuda by example.* Massachusetts: Addison Wesley; 2011.
- [30] Martins PJM. *Imaging Techniques in RPC-PET [dissertation].* University of Coimbra, Portugal; 2014.
- [31] Hebert TJ, Leahy R. Fast methods for including attenuation in the EM algorithm. *IEEE Trans Nucl Sci.* 1990 Apr;37(2):754–758.
- [32] Comtat C, Kinahan PE, Defrise M, et al. Fast reconstruction of 3D PET data with accurate statistical modeling. *IEEE Trans Nucl Sci.* 1998 Jun; 45(3):1083–1089.
- [33] Levkovitz R, Falikman D, Zibulevsky M, et al. The design and implementation of COSEM, an iterative algorithm for fully 3-D listmode data. *IEEE Trans Med Imag.* 2001 July;20(7):633–642.
- [34] Snyder DL, Miller M. The use of sieves to stabilize images produced with the em algorithm for emission tomography. *IEEE Trans Nucl Sci.* 1985 Oct; 32(5):3864–3872.
- [35] Tong S, Alessio AM, Kinahan PE. Noise and signal properties in PSF-based fully 3D PET image reconstruction: an experimental evaluation. *Phys Med Biol.* 2010;55(5):1453.